A *W*-Band Polarization Converter and Isolator

Charles Dietlein, *Student Member, IEEE*, Arttu Luukanen, *Member, IEEE*, Zoya Popović, *Fellow, IEEE*, and Erich Grossman, *Member, IEEE*

***Abstract*—A 95-GHz printed low-loss linear-to-circular polarizer is designed as a component of an active direct-detection millimeter-wave imaging system. The periodic printed grid structure presents different reactances to the TE and TM polarizations, resulting in equal amplitude and phase quadrature upon transmission through four parallel grids. The polarizer is measured in both a Gaussian beam system and a plane wave system, and demonstrates an axial ratio of 0.23 dB, polarization isolation of 38 dB, and transmission loss of 0.3 dB for normal incidence. The quarter-wave plate is characterized up to $\pm 35°$ off the optical axis, and exhibits an axial ratio better than 1 dB up to $\pm 17°$ off the optical axis.**

***Index Terms*—Millimeter wave devices, millimeter wave imaging, polarization.**

I. Introduction

SINCE the late 1980s, both passive and active millimeter-wave and submillimeter-wave imaging have gained attention for applications such as concealed weapons detection (CWD) [1], remote sensing [2], inclement-weather navigation, large-scale fire detection, material measurements, spectroscopy, radio astronomy, and plasma diagnostics [3, pp. 342–536].

Many of the systems contain various passive quasi-optical components described in [3, pp. 71–229], such as lens systems with Gaussian beams, dielectric lenses, anti-reflection coatings, metallic lenses, reflective focusing elements, delay lines, polarization processing, wave plates, absorbers and calibration loads, and a variety of frequency-selective surfaces and gratings.

This paper describes a low-loss, high-scan-angle, printed, low-cost *W*-band linear-to-circular polarizer (quarter-wave plate) designed for an active CWD system [4] developed at the National Institute of Standards and Technology (NIST) in Boulder, CO.

A simplified block diagram of the system is shown in Fig. 1. The target is illuminated by a $400\lambda_o$-long 1-D antenna array ($f_o = 95$ GHz). The linearly polarized (LP) illumination beam is focused by a cylindrical lens, reflected from a polarizing beam splitter and circularly polarized (CP) by the $\lambda/4$ plate; the resulting CP wave illuminates the target at various illumination angles due to the video-rate scanning mirror. The resulting scattered wave is orthogonally circularly polarized, and thus upon passing through the $\lambda/4$ plate becomes orthogonally linearly polarized to the illuminating wave. The wave then passes through the polarizing beam splitter and is sampled by a 1×128 room-temperature antenna-coupled microbolometer array [5]. Therefore, in this configuration, the $\lambda/4$ plate is critical not only to produce circular polarization, but also to ensure isolation between the input and image-forming waves. The field of view required by the system, explained in [4], is 0.9 m by 1.8 m at a distance from the entrance aperture of 1.5 m. This corresponds to an opening angle of approximately $\pm 31°$.

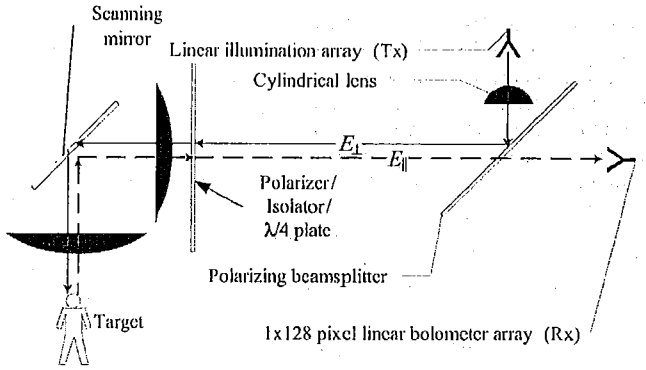

Fig. 1. Top view of simplified block diagram for the active CWD system. Shown is a cross section; the 1-D arrays are perpendicular to the plane of the paper. To the right of the $\lambda/4$ plate, $E_\parallel$ and $E_\perp$ are the two orthogonal linear polarizations, one parallel and one perpendicular to the plane of the paper.

A number of linear-to-circular polarizers have been demonstrated in the literature: single- and multiple-layer dipole arrays [6]–[8], layered dielectric frequency-selective surfaces [9], [10], metallic meander-lines [11]–[13], and finally, designs using combinations of capacitive and inductive grids [14], [15]. The last was chosen due to the advantages that it is quick to simulate, simple to fabricate (especially given the large aperture required), and performs well for this application.

This paper is organized as follows.

- Section II presents the design of a four-layer printed inductive-capacitive polarizer using a method-of-moment (MoM) and transmission-line simulation;
- Section III describes the low-cost fabrication process;
- Section IV details the measurement procedure and results;
- Finally, Section V discusses the effect of the quality of the polarizer on the CWD system performance.

II. Design and Simulation

This section describes the design of a unit cell of the polarizer, utilizing a combination of MoM and transmission-line analysis.

Manuscript received June 23, 2006; revised November 14, 2006. This work was supported by the National Science Foundation, by Award #0501578, and by both the U.S. National Institute of Standards and Technology (NIST) and by the U.S. Department of Commerce.

C. Dietlein and Z. Popović are with the Department of Electrical and Computer Engineering, University of Colorado, Boulder, CO 80309 USA (e-mail: dietlein@colorado.edu).

A. Luukanen was with the U.S. National Institute of Standards and Technology (NIST). He is now with VTT MilliLab, Espoo, Finland (e-mail: arttu.luukanen@vtt.fi).

E. Grossman is with the National Institute of Standards and Technology (NIST), Boulder, CO 80305 USA (e-mail: grossman@boulder.nist.gov).

Color versions of one or more of the figures in this paper are available online at http://ieeexplore.ieee.org.

Digital Object Identifier 10.1109/TAP.2007.898595

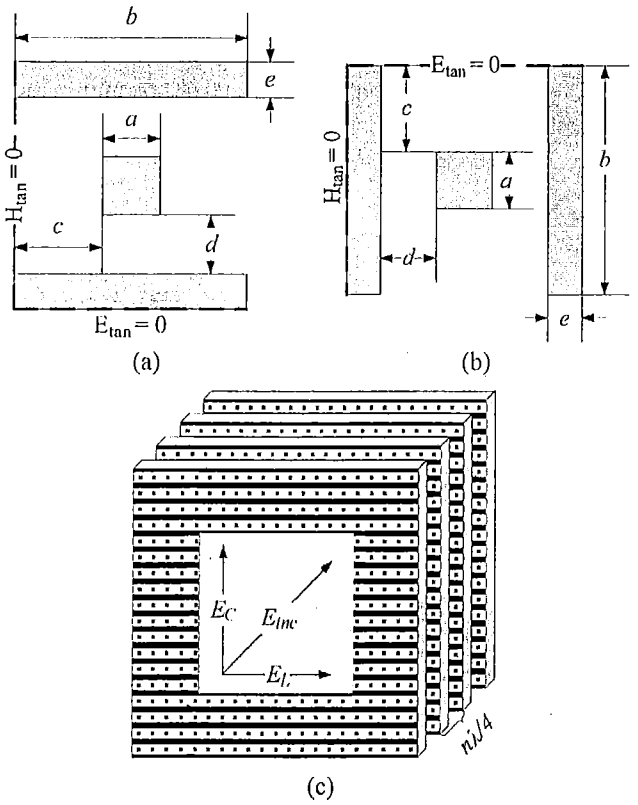

Fig. 2. (a) Parametrization of polarizer unit cell for E_C vector, with dimensions $a = 0.63$ mm, $b = 1.263$ mm, $c = 0.5$ mm, $d = 0.525$ mm, $e = 0.21$ mm. Electric and magnetic walls are indicated by $E_{tan} = 0$ and $H_{tan} = 0$, respectively. (b) Unit cell for E_L vector. (c) Layering of sheets and superpose of electric field vector orientation—Incident electric field E_{inc} is oriented at 45° from the metal strips and decomposed into two orthogonal vectors (E_L and E_C). The spacing between sheets is $n\lambda/4$, with n odd.

A. Basic Principle of Operation

It is well known that metal strips present an equivalent inductance to an incoming copolarized wave, while perpendicular metal strips present a capacitance to an incoming plane wave: this inductance and capacitance can be calculated from the quasi-static approximation [16], and measurements have been shown to agree very well with calculation.

In order to achieve circular polarization, a 90° phase shift is required between two equal-magnitude orthogonal vector components of the electric field. This usually requires several grids with a more complex unit cell. The unit cell in this paper is shown in Fig. 2(a) and (b) for two orthogonal electric field vector components.

For normal incidence and an infinite 2-D grid surface in the xy plane, symmetry defines electric and magnetic wall boundary conditions extending in the $\pm z$ direction. The magnetic walls are the vertical sides of the unit cell and the electric walls are the horizontal sides. This simplification of the geometry allows the polarizer design to be reduced to the design of a single unit cell, decreasing simulation complexity and time. A number of methods can be used to this end, the discussion of which is not the topic of this paper. The design tool used for this work was an available subdomain Galerkin MoM code, described in detail in [17].

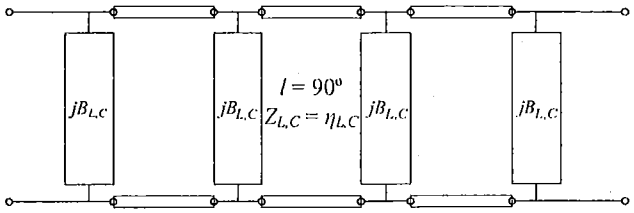

Fig. 3. Equivalent transmission-line circuit model for E_L and E_C polarizations. The susceptance blocks for each polarization are imported from the MoM simulation.

Definitions for angular quantities and S-parameter notation are as follows:

- S_{21}^C: The transmission coefficient of the E_C component through the polarizer;
- S_{21}^L: Similarly, the transmission coefficient of the E_L component through the polarizer;
- ϕ: Phase difference between S_{21}^C and S_{21}^L;
- θ: Off-normal angle of incidence;
- ψ: Polarizer rotation about optical axis z.

B. Simulation

S-parameters are extracted from the MoM simulations of the unit cells for both polarizations, and imported into Agilent Advanced Design System [18]. Four identical grids are cascaded with sections of $\lambda_o/4$-long sections of air between them, depicted in Fig. 2(c). The equivalent transmission line model for the two polarizations is shown in Fig. 3. The susceptances, jB_L and jB_C, are due to the following: the electric field vector oriented along the strips, E_L, is presented with an inductance due to the strips and a capacitance due to the squares; the electric field vector perpendicular to the strips, E_C, is presented with capacitances due to both the strips and squares, and capacitances due to the strips alone. The metallic grids are printed on a substrate with electrical thickness less than $\lambda_o/60$; therefore the substrate is ignored in simulation. A standard S-parameter simulation is completed between 90–100 GHz for both orthogonal components of the electric field. Optimization was performed for equal magnitude between S_{21}^C and S_{21}^L, and $\phi = 90°$. The dimensions of the unit cells were varied in the MoM code to adjust the capacitance and inductance empirically until circular polarization was reached at the center frequency. Comparison of simulation and measurement of the two-port S-parameters for jB_C is given in Section IV B.

Since the unit cell has a rectangular transverse cross-section, the impedances of the transmission lines used in the simulation are $\eta_L = \eta_0 b/(2e+2d+a) = \eta_0 b/A$ and $\eta_C = \eta_0 A/b$, where b and A are dimensions of the unit cell between electric and magnetic walls, respectively, and η_o is the impedance of free space [19].

III. Fabrication

A DuPont Pyralux AP8515RA [18] polyimide substrate with thickness $h = 25.4$ μm and Cu thickness $t = 18$ μm is used. The sheets are fabricated with a standard commercial wet-etch process, at a relatively low cost. The relative dielectric constant of the substrate is $\epsilon_r = 3.2$. Each of the four grids is 53.3 cm in diameter. Three sheets of rigid, low-density, $3\lambda/4$-thick, low-ϵ_r,

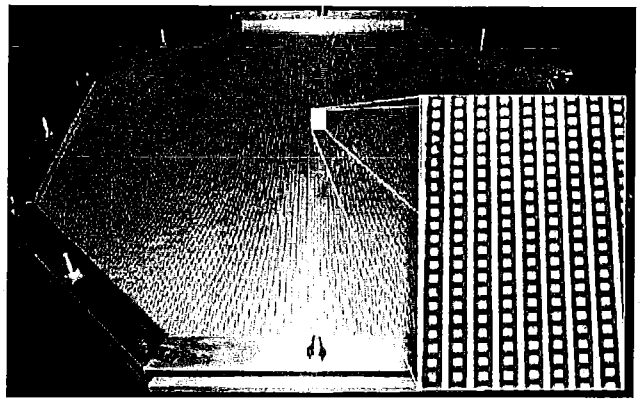

Fig. 4. Photograph of fabricated and assembled polarizer with octagonal aluminum frame. The aperture is 53 cm in diameter. Inset: a magnification of the photograph to show the pattern detail.

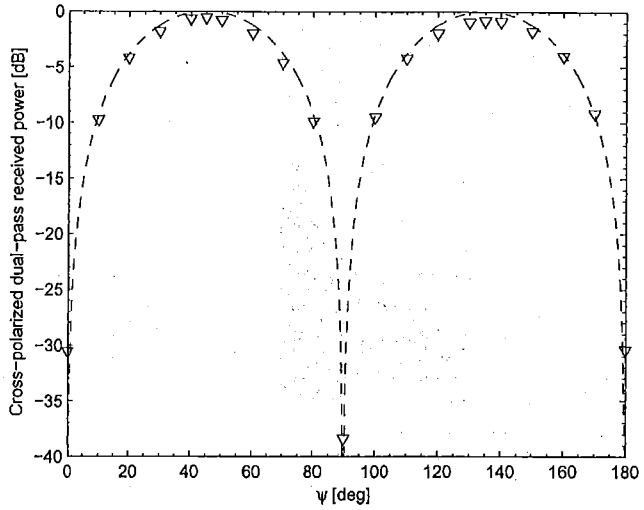

Fig. 5. Measured cross-polarized received power after two passes through the polarizer, as a function of polarizer rotation angle ψ about the optical axis z. Single-pass insertion loss is 0.3 dB, and polarization isolation is 38 dB. Measured data are denoted by ∇, while the theoretical $\sin^2(2\psi)$ is represented by a dashed line. Measured data are normalized to the power received without the polarizer in the optical path.

low-tan δ Cuming C-Stock RH-5 [18] (complex relative permittivity of $\epsilon/\epsilon_0 = 1.09 - j0.00044$) foam are sandwiched between the four polarizer sheets, while an extra foam layer is added behind the last polarizer sheet to provide additional stability and flatness. The completed polarizer is supported by an aluminum frame, as shown in Fig. 4.

A 53-cm diameter clear aperture is required, due to the optics specifications of the imaging system. The corresponding dielectric lenses, mirrors, polarizing beamsplitters, and transmit/receive modules in the system (see Fig. 1) have apertures of similar sizes.

IV. Testing and Performance

This section details the two testing methods used to measure the performance of the polarizer, and provides comparison between measurement and simulation.

A. Insertion Loss and Isolation

A dual-pass reflection power measurement is performed to measure polarization rotation and isolation. A Gunn diode oscillator tuned to $f = 95$ GHz feeds a standard-gain horn antenna that transmits a wave at the polarizer backed by a mirror. The incidence angle is slightly off-normal ($\theta \approx 5°$) to allow measurement of the reflected power. A power meter attached to an identical horn antenna is placed close to the source at the corresponding angle slightly off-normal to measure the reflected power. The two horns are cross polarized, and the polarizer is rotated 180° about the optical axis on a rotation stage with a 45-mm-clear aperture to the polarizer. RF absorber is cut to form the aperture and eliminate stray reflections from the polarizer frame.

The measured power as a function of rotation angle is shown in Fig. 5 and compared to the theoretical $\sin^2(2\psi)$. The measurement is normalized with respect to the received power without the polarizer in the optical path. The measured single-pass insertion loss is 0.3 dB, and the isolation between the two polarizations is 38 dB.

B. Gaussian Beam Measurement

An HP 8510C network analyzer is configured with the 85105A millimeter-wave test set and W85104A W-band extension heads [18]. The heads are attached to short W-band waveguide sections, followed by corrugated conical horn antennas with beam waist $w_0 = 7.1$ mm at $f = 95$ GHz. Bi-convex dielectric lenses with focal depth $d = 15.2$ cm and $\epsilon_r = 3.1$ are added to form a copolarized Gaussian beam measurement system. A response-isolation calibration for S_{21} is performed between 90–100 GHz, and the optics optimized based on the desired beam radius at the polarizer measurement plane. The system is a standard Gaussian beam configuration, such as in [20].

Due to the physical size of the completed polarizer for installation in the imaging system, a small 10-cm-diameter sample is utilized for testing. An acrylic frame is used to minimize reflections. A translation stage along the optical axis z and a rotation stage for ψ and θ support the polarizer sample. A separate translation stage without ψ rotation supports a single sheet of the fabricated pattern for measurement comparison with the MoM results.

An initial measurement set is taken, and standing waves are found to dominate the signal. Standing waves exist in the system due to two main reasons: lack of antireflection coatings on all components, and polarization-dependent reflections. Two standing waves are noticed—one between the apertures of the scalar feeds, and the second between the lenses and polarizer. RF absorber applied around the aperture edges of the horns reduces the amplitude of the lower-frequency standing wave. An attempt to eliminate the second standing wave was made by performing another measurement set with the polarizer sample rotated to a slight off-normal angle $\theta = 5°$, which reduced the second standing wave slightly. The remaining standing waves are eliminated by smoothing the data with a moving-average algorithm based on the period of the standing waves.

Fig. 6 shows the simulation results for a single grid in the E_C polarization compared to measured data. It should be noted that the absolute value of the phase is not relevant, but rather

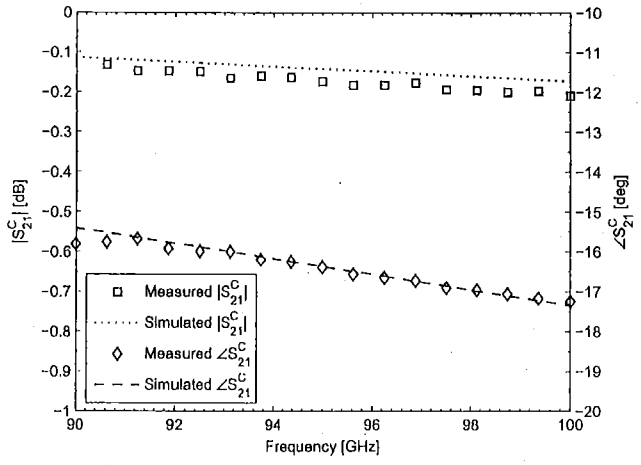

Fig. 6. Simulated S_{21}^C compared with measured magnitude (□) and phase (◇) of the transmission coefficient for a single sheet of the polarizer. Measured phase was shifted by several degrees to agree with simulation, due to absolute phase not being available in measurement.

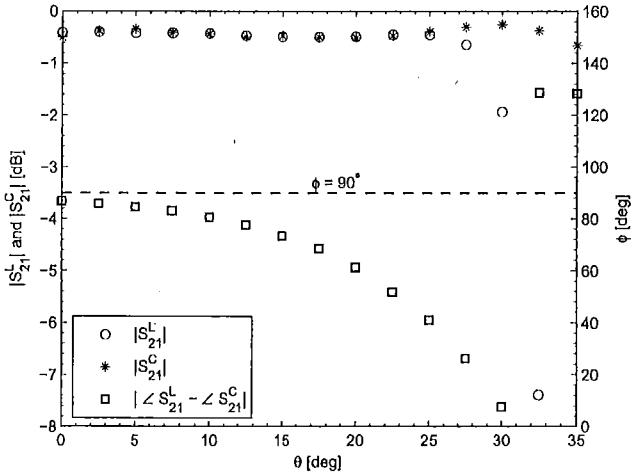

Fig. 7. Measured magnitude of S_{21}^C (○) and S_{21}^L (∗) as a function of off-normal rotation angle θ. While S_{21}^C stays relatively flat throughout the θ rotation, S_{21}^L rapidly decreases after $\theta = 25°$. Also shown is the phase difference ϕ between S_{21}^C and S_{21}^L as a function of θ, represented by □. Ideal phase difference $\phi = 90°$ is shown by the dashed line.

the slope of the phase as a function of frequency. The phase of the measured data is shifted slightly to allow easy comparison of the two slopes. The measured data closely match the simulation, with only the transmission loss being slightly higher than simulated.

In Fig. 7, $|S_{21}|$ through the capacitive and inductive orientations of the polarizer is shown. Ideally, the polarizer would have good off-axis performance, but due to the layered nature of this type of design, it is known that performance suffers at large angles. However, it is noted that the magnitude of the electric field for the two orientations remains constant (and nearly equal) up to $\theta = 25°$. Fig. 7 also shows the phase difference ϕ between the transmission coefficients S_{21}^C and S_{21}^L of the electric field, as a function of off-normal angle of incidence. For $\theta < 10°$, ϕ remains above 80°.

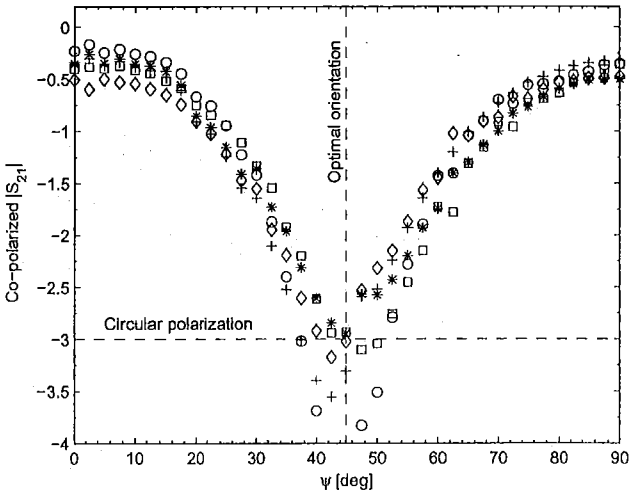

Fig. 8. Total measured transmission coefficient through the polarizer as a function of polarizer rotation angle ψ for 93.5–96.5 GHz in 750 MHz steps: ○, +, ∗, □, and ◇, respectively. $\psi = 0°$ and $\psi = 90°$ correspond to the E_L and E_C orientations, respectively.

Fig. 8 shows the total copolarized transmission coefficient as a function of polarizer rotation angle ψ at five frequencies from 93.5–96.5 GHz. The polarizer is designed to produce circular polarization when rotated so the metal strips are at $\psi = 45°$ relative to the direction of polarization of an incident electric field, i.e., any LP antenna in the circularly polarized field will exhibit 3 dB loss. At 0° and 90° the copolarized transmission loss is ideally 0 dB. Fig. 8 shows that the $\lambda/4$ plate performs as expected over a 5% bandwidth around 95 GHz, the frequency regime where the IMPATT source utilized by the system is centered.

C. Axial Ratio Calculation

Usually the axial ratio is defined as the ellipticity of the polarization ellipse, which is measured by rotating a LP horn in a circularly polarized field and recording the received electric field amplitude. Because it is not possible to rotate one of the horns in the Gaussian beam test, due to the size of the W85104A *W*-band extension heads, the phase-amplitude method is used for calculation of the axial ratio. In this method, phase information compensates for antenna rotation. The axial ratio is computed using the following:

$$AR = \left| \frac{\xi + 1}{\xi - 1} \right| \tag{1}$$

with

$$\xi = \sqrt{\frac{1 + a^2 + 2a \sin \phi}{1 + a^2 - 2a \sin \phi}} \tag{2}$$

where a and ϕ are the absolute value and angle of the ratio between two orthogonal components of the electric field, i.e.,

$E_o^1/E_o^2 = a\exp(j\phi)$. E_o^1 and E_o^2 should be measured simultaneously with a dual-linear polarized receive antenna for the above method to be exact. To check the validity of the approach, three measurement sets of orthogonal linear polarizations were taken, and the magnitude difference and relative phase between the measurement sets varied less than 1.5%. This implies that the axial ratio calculation obtained from separate linear polarization measurements can be trusted.

In the Gaussian beam measurement using S_{21}^L and S_{21}^C as the orthogonal component measurements in the above formulas, an axial ratio of 0.23 dB is calculated for normal incidence. As the angle of incidence is changed, the relative magnitudes of S_{21}^L and S_{21}^C remain similar up to $\theta = 25°$ (Fig. 7), but ϕ changes rapidly. Therefore, an axial ratio below 1 dB is maintained for angles of incidence $\theta < 17.5°$, and remains below 3 dB up to $\theta = 22.5°$.

V. Discussion

The concealed weapons detection system described in the introduction is limited by its signal to noise ratio, due to both the lack of transmitted power in this frequency band and decreased sensitivity of room-temperature bolometers. Therefore, it is essential to minimize insertion loss of all components. The 0.3–0.5 dB loss of the polarizer shown here saves 2.5 dB of signal relative to a system with no polarizer. In addition, high polarization isolation between the transmit and receive waves reduces effects of unwanted reflections, and thus improves the SNR of the image.

For the configuration shown in Fig. 1 with the polarizer between the polarizing beamsplitter and the dielectric lens, the required field of view is not greater than 20°. As the axial ratio of the polarizer degrades rapidly after 17°, images will appear "blurred" at the edges, due to non-CP reflections from the extremities of the target field plane. It is also possible to optimize the polarizer for off-axis performance, to achieve optimum axial ratio at, e.g., 15° off broadside. In this case, the *average* performance of the device would be increased, but an interesting and detrimental visual effect would be encountered. An annulus of high-quality imagery would be observed, with performance degrading monotonically both towards the center and the edges of the field of view. We have considered this tradeoff and decided in favor of optimum performance at broadside.

In summary, this paper presents a low-loss, low-cost, relatively high-scan-angle linear-to-circular polarizer at 95 GHz. The performance of this quasi-optical component results in improved images from the system for which it was designed.

References

[1] A. Luukanen, A. J. Miller, and E. N. Grossman, "Passive hyperspectral terahertz imagery for security screening using a cryogenic microbolometer," *Proc. SPIE*, vol. 5789, pp. 127–134, May 2005.

[2] H. Süss, K. Grüner, and W. J. Wilson, "Passive millimeter-wave imaging—A tool for remote sensing," *Alta Frequenza*, vol. 58, no. 5–6, Sep.–Dec. 1989.

[3] P. Goldsmith, *Quasioptical Systems*. Piscataway, NJ: IEEE, 1998, pp. 71–229, 324–536.

[4] E. N. Grossman, A. Luukanen, and A. J. Miller, "Terahertz active directdetection imagers," *Proc. SPIE*, vol. 5411, pp. 68–77, Sep. 2004.

[5] A. J. Miller, A. Luukanen, and E. N. Grossman, "Micromachined antenna-coupled uncooled microbolometers for terahertz imaging arrays," *Proc. SPIE*, vol. 5411, pp. 18–24, Sept. 2004.

[6] K.-S. Min, J. Hirokawa, K. Sakurai, M. Ando, and N. Goto, "Singlelayer dipole array for linear-to-circular polarisation conversion of slotted waveguide array," *Inst. Elect. Eng. Proc.-Microw. Antennas Propag.*, vol. 143, no. 3, pp. 211–216, Jun. 1996.

[7] S. Hollung and Z. Popović, "A quasi-optical isolator," *IEEE Microw. Guided Wave Lett.*, vol. 6, no. 5, pp. 205–206, May 1996.

[8] W. A. Shiroma, S. C. Bundy, S. Hollung, B. D. Bauernfeind, and Z. B. Popović, "Cascaded active and passive quasi-optical grids," *IEEE Trans. Microw. Theory Tech.*, vol. 43, no. 12, pp. 2904–2909, Dec. 1995.

[9] J. Bornemann, "Computer-aided design of multilayered dielectric frequency-selective surfaces for circularly polarized millimeter-wave applications," *IEEE Trans. Antennas Propag.*, vol. 41, no. 11, pp. 1588–1591, Nov. 1993.

[10] H. L. Bertoni, L. S. Cheo, and T. Tamir, "Frequency-selective reflection and transmission by a periodic dielectric layer," *IEEE Trans. Antennas Propag.*, vol. 37, no. 1, pp. 78–83, Jan. 1989.

[11] L. Young, L. Robinson, and C. Hacking, "Meander-line polarizer," *IEEE Trans. Antennas Propag.*, vol. 21, no. 3, pp. 376–378, May 1973.

[12] T.-K. Wu, "Meander-line polarizer for arbitrary rotation of linear polarization," *IEEE Microw. Guided Wave Lett.*, vol. 4, no. 6, pp. 199–201, 1994.

[13] E. Ongareau, A. Roussaud, E. Marouby, and J.-R. Levrel, "Radar cross-section reduction by polarization rotatoin," *Microw. Opt. Technol. Lett.*, vol. 8, no. 6, pp. 316–318, Apr. 1995.

[14] D. S. Lerner, "A wave polarization converter for circular polarization," *IEEE Trans. Antennas Propag.*, vol. 13, no. 1, pp. 3–7, Jan. 1965.

[15] K. M. K. H. Leong and W. A. Shiroma, "Waffle-grid polariser," *Inst. Elect. Eng. Electron. Lett.*, vol. 38, no. 22, pp. 1360–1361, Oct. 2002.

[16] G. G. MacFarlane, "Quasi-stationary field theory and its application to diaphragms and junctions in transmission lines and wave guides," in *Proc. Inst. Elect. Eng. London*, U.K., 1946, vol. 93, pp. 703–719.

[17] S. C. Bundy and Z. B. Popović, "A generalized analysis for grid oscillator design," *IEEE Trans. Microw. Theory Tech.*, vol. 42, no. 12, pp. 2486–2491, Dec. 1994.

[18] US Department of Commerce disclaimer: Any mention of commercial products or reference to commercial organizations is for information only; it does not imply recommendation or endorsement by NIST nor does it imply that the products mentioned are necessarily the best available for the purpose..

[19] Z. Popović, "Grid oscillators," Ph.D. dissertation, , Calif. Inst. Technol., Pasadena, 1990.

[20] T.-K. Wu, *Frequency Selective Surface and Grid Array*. New York: Wiley, 1995, pp. 13–14.

Charles R. Dietlein (S'99) received the B.S. degree in electrical engineering from Seattle Pacific University, Seattle, WA, in 2003, and the M.S. degree in electrical engineering from the University of Colorado at Boulder in 2005.

He is currently a Graduate Research Assistant with the University of Colorado at Boulder, working toward the Ph.D. degree. His research interests include active room-temperature and passive cryogenic millimeter-wave/THz imaging, measurement, and calibration techniques for both 300 and 4 K millimeter-wave/THz detectors, and broadband/multispectral image phenomenology.

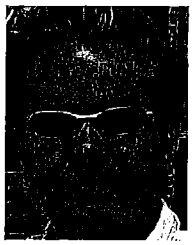

Arttu Luukanen (M'05) was born in 1972 in Finland. He received the M.Sc. degree from the University of Helsinki, Finland, in 1999, and the Ph.D. degree in 2003 from the University of Jyväskylä, Finland, both in applied physics.

From 1994 to 2000, he was a Research Assistant and, later, a Research Scientist with Metorex International Oy, Finland, where he worked on the development of X-ray instruments for several space science missions of ESA, NASA, and NASDA. After his graduate studies in 2003, he joined the VTT Technical Research Centre of Finland as a Research Scientist. From late 2003 until 2005, he visited the Quantum Electrical Metrology Division of the National Institute of Standards and Technology, Boulder, CO. During this time, his research focused on the development of both active and passive THz imaging systems for security applications. In 2005, he was nominated as the director

of MilliLab—the Millimetre-wave Laboratory of Finland. His research focuses on the development of various direct detectors of mm-wave and terahertz radiation, passive THz imaging arrays for security applications, as well as novel THz source technologies.

Dr. Luukanen is the Chair of the Finland AP-03/ED-15/MTT-17 societies.

Zoya Popović (S'86–M'90–SM'99–F'02) received the Dipl. Ing. degree from the University of Belgrade, Serbia, Yugoslavia, in 1985, and the Ph.D. degree from the California Institute of Technology, Pasadena, in 1990.

Since 1990, she has been with the University of Colorado at Boulder, where she is currently a Full Professor. She has developed five undergraduate and graduate electromagnetics and microwave laboratory courses and coauthored the textbook *Introductory Electromagnetics* (Englewood Cliffs, NJ: Prentice-Hall, 2000) for a junior-level core course for electrical and computer engineering students. Her research interests include microwave and millimeter-wave quasi-optical techniques, high-efficiency microwave circuits, smart and multibeam antenna arrays, intelligent RF front ends, RF optical techniques, batteryless sensors, and broadband antenna arrays for radio astronomy.

Dr. Popović was the recipient of the 1993 Microwave Prize presented by the IEEE Microwave Theory and Techniques Society (IEEE MTT-S) for the Best Journal Paper. She received the 1996 URSI Isaac Koga Gold Medal. In 1997, Eta Kappa Nu students chose her as a Professor of the Year. She was the recipient of a 2000 Humboldt Research Award for Senior U.S. Scientists from the German Alexander von Humboldt Stiftung, as well as the 2001 Hewlett-Packard (HP)/American Society for Engineering Education (ASEE) Terman Award for combined teaching and research excellence.

Erich N. Grossman (M'87) received the A.B. degree from Harvard College, Cambridge, MA, in 1980, and the Ph.D. degree, both in physics, from the California Institute of Technology, Pasadena, in 1987. His thesis work involved the construction and testing of an ultralow noise, far-infrared heterodyne receiver for airborne astronomy, using cryogenic Ge:Ga photomixers.

From 1988 to 1989, he was a Postdoctoral Fellow with the University of Texas at Austin, working jointly in the Astronomy and Electrical Engineering Departments. In 1989, he joined the National Institute of Standards and Technology (NIST), Boulder, CO, where he is a Physicist in the Optoelectronics Division working in the field of infrared and submillimeter device physics. Notable accomplishments at NIST include the development and experimental demonstration of the world's highest frequency, high-efficiency lithographic antennas, of the world's highest frequency Josephson junctions, and original conception and development of the SQUID multiplexer, enabling for the first time large arrays of ultralow-noise superconducting detectors.

Dr. Grossman was awarded a Department of Commerce Gold Medal in 1993.